PCCP

Accepted Manuscript

ROYAL SOCIETY OF CHEMISTRY

www.rsc.org/pccp

Morphologic dependence of silver electrodeposits by changing the ionic liquid solvent and the deposition parameters: Experimental and modelling approaches†

Francisco A. A. Figueredo-Sobrinho,[a] Luis P. M. Santos,[a] Davi S. Leite,[a] Diego C. Craveiro,[a] Samir H. Santos,[b] Katlin I. B. Eguiluz,[b] Giancarlo R. Salazar-Banda,[b] Cleiton D. Maciel,[c] Maurício D. Coutinho-Neto,[c] Paula Homem-de-Mello,[c] Pedro de Lima-Neto[a] and Adriana N. Correia*[a]

[a] *Departamento de Química Analítica e Físico-Química, Centro de Ciências, Universidade Federal do Ceará, Bloco 940 Campus do Pici, 60440-900, Fortaleza-CE, Brazil*

[b] *Instituto de Tecnologia e Pesquisa/Programa de Pós-Graduação em Engenharia de Processos, Universidade Tiradentes, 49032-490, Aracaju-SE, Brazil*

[c] *ABCSim, Centro de Ciências Naturais e Humanas, Universidade Federal do ABC, Avenida dos Estados, 5001, Bloco B, sala 1017, 09210-580, Santo André-SP, Brazil*

***Corresponding author.** Profa. Dra. Adriana N. Correia.
E-mail address: adriana@ufc.br
Telephone: +55 85 3366 9050

† Electronic supplementary information (ESI) available: EDS, SEM and XRD data.

Abstract

The low toxic and environmentally compatible ionic liquids (ILs) are alternatives to the toxic and harmful cyanide-based baths used in industrial silver electrodeposition. Here, we report the successfully galvanostatic electrodeposition of silver films using the air and water stable ILs 1-ethyl-3-methylimidazoliumtrifluoromethylsulfonate ([EMIM]TfO) and 1-H-3-methylimidazolium hydrogen sulphate ([$HMIM^+$] [HSO_4^-]) as solvents and AgTfO as the source of silver. The electrochemical deposition parameters were thoughtfully studied by cyclic voltammetry before deposition. The electrodeposits were characterized by scanning electron microscopy coupled with X-ray energy dispersive spectroscopy and X-ray diffraction. Molecular dynamics (MD) simulations were used to investigate the structural dynamic and energetic properties of AgTfO in both ILs. Cyclic voltammetry experiments revealed that the reduction of silver is a diffusion-controlled process. The morphology of the silver coatings obtained in [EMIM]TfO is independent of the applied current density, resulting in nodular electrodeposits grouped as crystalline clusters. However, the current density significantly influences the morphology of silver electrodeposits obtained in [$HMIM^+$][HSO_4^-], thus evolving from dendrites at 15 mA cm^{-2} to the coexistence of dendrites and columnar shapes at 30 mA cm^{-2}. These differences are probably due to the greater interaction between Ag^+ and [HSO_4^-] than with TfO^-, as indicated by the MD simulations. The morphology of Ag deposits is independent of the electrodeposition temperature for both ILs, but, its increasing increases the cluster sizes. Pure face-centred cubic polycrystalline Ag was deposited in the films with crystallite sizes in nanometre scale. The morphologic dependence of Ag with the current density applied using the [$HMIM^+$][HSO_4^-] IL opens up the opportunity to produce different and predetermined Ag deposits.

1. Introduction

Electrodeposition processes are widely used in the industry from decorative and aesthetic purposes to corrosion protection purposes. Aqueous electrolytes are commonly employed in this process, which have some limitations, such as narrow potential windows, gas evolution, the use of complexing agents and high environmental impact, since the effluents eventually need to be discarded[1]. As an alternative, different electrolytes have been proposed, such as organic solvents, thus eliminating some of the problems existing in that media. However, the high volatility, toxicity and handling complications of these solvents make their use unfavourable for industrial uses[1,2].

In recent years, ionic liquids (ILs) have been extensively used in the electrodeposition of metals[3–5]. The ILs are compounds which melt at temperatures below 100 °C and fit in the concepts of green chemistry, because of their low vapour pressure, low toxicity, high thermal stability and moderate polarity; thus, they may be employed in certain processes which use significant amounts of toxic solvents[3,6]. Due to their low toxicity and their environmental compatibility, ILs offer an alternative to the toxic cyanide-based baths used for electroplating[7]. Moreover, its high thermal stability combined with its low vapour pressure, makes possible their use in open galvanic baths at varying temperatures without release of toxic vapour, which reduces the amount of volatile organic compounds released into the atmosphere[8,9].

Moreover, some studies have shown that the use of ILs as electrolytes favours the electrodeposition of nanocrystalline materials, which in aqueous medium requires the use of pulsed electrodeposition and/or the addition of additives, which usually significantly affects the reaction mechanism[1,10]. In addition, several studies have highlighted the importance of ILs as a versatile tool for the electrodeposition of nanostructured materials[11,12].

Aprotic and protic ILs are formed by various proton transfer and association equilibria from Brønsted acid to Brønsted bases[13,14]. Protic ILs can be synthesized at lower costs due to its simple synthetic route, which employs reagents such as amines and acids that have well-known properties, such as low toxicity, biodegradability, and low cost and environmental impacts. Moreover, they tend to have higher fluidity and conductivity than aprotic ILs for reasons that are not yet well defined[1,15]. Studies have shown the potential of protic ILs as electrolytes in electrochemical systems, specifically in fuel cells and electrodeposition of conducting polymers[1,16–18]. However, their use as electrolytes in the electrodeposition of metals is scarce.

The deposition of silver coatings has been intensively studied since it is a noble material mainly used in very thin layers[19,20]. The industries of microelectronics materials, aerospace, automotive and jewellery require thin, homogeneous and good looking silver layers, which may be obtained from its deposition on a less noble substrate at low cost[21].

However, the electroplating baths used on industrial scale for the silver electrodeposition are extremely toxic, because of its high cyanide content. These cyanide-based additives form a complex compound with Ag^+ ions, thus preventing their spontaneous reduction. However, besides the presence of cyanide is undesirable in aquatic environments, it is harmful to the bath operator[20]. Moreover, the treatment of its effluent and disposal of wastewater requires appropriate technologies at a high cost[20]. The use of ILs as solvents in the electrodeposition of silver has replaced toxic cyanide-based electroplating baths[3,8,19,21]. Several aprotic ILs have been reported for silver electrodeposition, such as 1-butyl-3-methylimidazolium tetrafluoroborate ([BMIM][BF_4])[20–22], N-butyl-N-methyl-pyrrolidiniumbis(trifluoromethanesulfonyl)imide ([C_4mPyr][TFSI])[21], 1-ethyl-3-methylimidazolium trifloromethanesulfonate ([EMIM]TfO)[8,19], 1-butyl-3-methylimidazolium hexafluorophosphate ([BMIM][PF_6])[22,23], N-butyl-N-

methylpyrrolidiniumbis(trifluoromethanesulfonyl)imide ([BMP][TFSI])[24], N-butyl-N-methylpyrrolidiniumdicyanamide ([BMP][DCA])[24], ionic liquid microemulsions[10], 3-butylpiridinium bis(trifluoromethanesulfonyl)imide ([3-BuPyr][NTf_2])[7], [BMP][NTf_2][6], [BMI][NTf_2][6], [TMHA][NTf_2][6], [BMIM][TfO][6], 1-butyl-3-methylimidazolium bistriflimide ([BMIM][NTf_2])[11] and silver complex ionic liquids[25]. In addition, the electrodeposition of silver has also been carried out in protic ILs, such as ethylammonium nitrate (EAN)[1], triethylammoniummethylsulfonate ([Et_3N][$MeSO_4$]), TAMS[1], bis(2-methoxyethyl) ammonium acetate ([$(MeOEt)_2NH$][AcOH]), MOEAA[1], 1-methylpyrrolidinium acetate ([HMPyr][Ac])[12] and 1-methylpyrrolidinium nitrate ([HMPyr][NO_3])[12].

Despite the increasing use of ILs as electrolytes in electrodeposition of metals and alloys, the metals interaction with the ILs is still not well-established in the literature neither the role of these interactions on its electrochemical behaviour, which in turn can influence the morphology of coatings. To fill this gap, it is possible to use computational simulations of molecular dynamics as a tool to understanding the interaction between the solute and the ionic liquid, which provides an atomistic description of the system.

In this study, we report the electrodeposition of silver from room temperature aprotic and protic ILs. The aprotic IL, 1-ethyl-3-methylimidazolium trifluoromethylsulfonate ([EMIM]TfO) and the protic IL, 1-H-3-methylimidazolium hydrogen sulphate ([$HMIM^+$][HSO_4^-]) were used and their voltammetric profiles were evaluated. The electrochemical behaviour of silver in both ILs was investigated by cyclic voltammetry (CV) and the Ag deposits were examined by field emission gun-scanning electron microscopy (FEG-SEM), energy dispersive X-ray spectroscopy (EDS) elemental analysis and X-ray diffraction (XRD). The interaction between silver and each IL were evaluated by molecular dynamics (MD) simulations.

2. Experimental

2.1. Materials

The electrodeposition of silver was studied in the water and air stable ionic liquids [EMIM]TfO and [$HMIM^+$][HSO_4^-]. [EMIM]TfO was purchased from Sigma-Aldrich® while [$HMIM^+$][HSO_4^-] was previously synthesized following the methodology described by Carlesi Jara *et al.*[26]. Silver trifluoromethylsulfonate (Sigma-Aldrich, 99 %) was used as a source of silver due to its high solubility in the employed ILs. The solutions containing ILs were dried by heating under a vacuum at 120 ^oC and the content of residual water was less than 50 ppm after drying, checked using a coulometric Karl Fischer method (Metrohm 795 KTF Titrino). The analytical grade reagents were used as received without further purification or drying. Ultrapure water purified by a Millipore Waters System was used (18.2 MΩ cm at 25 ^oC).

2.2. Electrochemical measurements

All electrochemical measurements were performed using a computer-controlled AUTOLAB PGSTAT30 Potentiostat/Galvanostat (Metrohm-Eco Chemie). The data acquisition was carried out using the GPES 4.9 software. The electrochemical behaviour of AgTfO in the [EMIM]TfO and [$HMIM^+$][HSO_4^-] ILs was monitored by CV using a classical three-electrode setup consisting of a gold disk (0.08 cm^2) as working electrode, a Pt spiral as counter electrode and an Ag wire as pseudo-reference electrode.

Initially, the working potential range, in each IL, was determined through CV experiments that were carried out first for pure solvents and subsequently for the ILs containing 50 mmol L^{-1} AgTfO at scan rate of 50 mV s^{-1} and at room temperature. Hence, CV experiments were performed at room temperature in the selected potential range for each IL containing 50 mmol L^{-1} AgTfO at scan rates of 10, 25, 50 and 100 mV s^{-1}. The effect of

temperature on the electrochemical behaviour of AgTfO in both ILs was also investigated by CV experiments in the selected potential range at 50 mV s^{-1}, in the temperature range from 25 to 45 °C controlled by an ultra-thermostatic bath (CIENLAB).

For the silver electrodeposition, 0.42 cm^2 gold plates were used as working electrodes. Prior to electrodeposition the electrodes were cleaned with acetone in an ultrasonic bath (Quimis 0335D), rinsed with ultrapure water and dried with a nitrogen 4.6 gas flow (White Martin, Brazil 99.996%). The electrodeposition assays were performed by galvanostatic method at 15 or 30 mA cm^{-2} at 30 °C and 45 °C. For XRD analyses the silver coatings were deposited onto a 1.62 cm^2 glassy carbon (GC) electrode. The GC electrodes were polished with 0.3 μm diamond paste, and washed in acetone, ethanol and ultrapure water in an ultrasonic bath for 3 min, respectively, and followed by thoroughly rinsed with ultrapure water and dried in air.

The electrode potential of the reference electrode was calibrated in several experiments by using the ferrocene/ferrocenium redox couple (Fc/Fc^+) in CV experiments using a 2.5 mmol L^{-1} ferrocene (Fc) solution in [EMIM]TfO or [$HMIM^+$][HSO_4^-], in the temperature range from 25 to 45 °C. Therefore, all potentials hereafter will be referred to the Fc/Fc^+ couple, as suggested by Saheb *et al*.[27].

2.3. Physical characterisation

The surfaces of Ag deposits on gold plates were examined using FEG-SEM in a FEI-Quanta 450 FEG microscope with an Oxford EDS system operating at an accelerating voltage of 20 kV, as well as using a Vega XMU Tescan microscope for SEM analyses. XRD patterns of Ag deposited samples were obtained using a Philips X'Pert Pro diffractometer, in step scan mode with step size of 0.02° and using $Cu_{K\alpha}$ radiation. The measurements were carried out in the angular interval range from 30° to 70°. The samples were rinsed with Milli-Q water and

dried under a flow of inert gas prior to XRD and SEM investigations. XRD patterns were compared with files from the ICSD database.

2.4. Computational simulations

In order to support experimental observations, we applied extensive molecular dynamics simulations of AgTfO salt in [EMIM]TfO and [$HMIM^+$][HSO_4^-] ILs. Computational cubic cells were modelled for each ionic liquid containing 515 ion pairs and 50 and 30 AgTfO molecules in [EMIM]TfO or [$HMIM^+$][HSO_4^-], respectively. MD simulations were carry out in the isothermal-isobaric ensemble (NPT), where the pressure (p = 1 atm) and the temperature (T = 298K) were kept constant by using the Parrinello-Rahman[28] and V-rescale[29] schemes.

The parameters used in MD simulations for both ILs were developed in a systematic way by several groups,[30–32] based on OPLS-AA force field.[33] Parameters proposed for alkylsulphate (C_nSO_4) were used to model HSO_4 ion, replacing the group C_n by H and using a charge of 0.22 e.[34] Partial charges of [$HMIM^+$] cation were derivated from Chelpg method.[35] The set of parameters of Ag^+ was proposed by Spezia *et al.* validated in aqueous solutions simulations.[36]

Periodic boundary conditions and minimum image convention were applied[37]. The bond length was constrained via LINCS algorithm.[38] A cut-off of 1.2 nm was applied to van der Waals interactions, whereas the electrostatic interactions were treated by Particle Mesh Ewald method.[39] Computational cells were previously equilibrated for 50 ns. The thermodynamic properties were calculated after production phases of 100 ns with a time-step of 2 fs and a data collection every 0.01 ps. All the simulations were performed by using GROMACS 4.5 package.[40]

3. Results and discussion

3.1. Cyclic voltammetry studies

Figs. 1a and 1b show the background voltammograms (dashed curves) of the [EMIM]TfO and [$HMIM^+$][HSO_4^-] ILs, respectively, on Au disk electrode under atmospheric conditions and using different potential ranges. Both figures also show the voltammetric profiles for both ILs in the presence of AgTfO (solid curves). In general, ILs have large electrochemical windows, but the cation or the anion of the IL can suffer oxidation or reduction and these processes may occur in the same potential range of the reduction of the metal of interest. Thus, for the [EMIM]TfO IL (Fig. 1a) one reduction and one oxidation processes appear, which can be attributed to the reduction (peak a) and the oxidation (peak b) of the electrode substrate (gold) [21].

Figure 1

The cyclic voltammogram taken at 50 mmol L^{-1} AgTfO in [EMIM]TfO (solid curve in Fig. 1a) shows that the Ag reduction process occurred in a different potential range than the gold electrode reduction.

In the Fig.1b, none electrochemical process appears in the selected range used for the background voltammogram (dashed line). The voltammetric peak profile of the AgTfO in [$HMIM^+$][HSO_4^-] (solid curve in Fig. 1b) is consistent with the expected for metal deposition and stripping from an electrode surface (peaks a and b), similarly than the behaviour shown in Fig. 1a for the [EMIM]TfO IL (peaks c and d). Notably, the potential difference between the cathodic and the anodic potential peaks is lower for the [$HMIM^+$][HSO_4^-] than for the [EMIM]TfO IL, suggesting different electrodeposition behaviours.

CV experiments were carried out at different scan rates (from 10 to 100 mV s^{-1}) for each IL to verify the influence of the nature of the IL on the electrochemical behaviour of AgTfO, as well as to try to elucidate the mechanism involved in the electrodeposition of Ag

on Au surface in two different media. Figs. 2a and 2b show the scan rate (υ) effect on the electrodeposition process. The linear dependence between I_{rp} and $\upsilon^{1/2}$ displayed in the insets of both figures strongly suggest diffusion-controlled processes[21]. Linear coefficients unequal to zero which can be associated to changes in the electrode area during silver electrodeposition[21,41]. From the angular coefficient taken for the insets in Fig. 2 it was possible to calculate the diffusion coefficient (D) using the Randles-Sevcik equation.

Figure 2

Table 1 shows the diffusion coefficient of Ag^+ in [EMIM]TfO and $[HMIM^+][HSO_4^-]$ in $cm^2\ s^{-1}$. These data shows that the Ag^+ ion has a better mobility in the [EMIM]TfO than in $[HMIM^+][HSO_4^-]$ and this behaviour can be an important factor in its electrodeposition. The significant difference between the D values, about two orders of magnitude, can be explained by the different viscosity of the ILs. According to literature data, the values of dynamic viscosity of the [EMIM]TfO and $[HMIM^+][HSO_4^-]$ are 52 and 923 mPa at 25 °C, respectively[5,26]. Thus, the higher the viscosity the lower the D values.

Table 1

Table 1 also shows voltammetric data for reduction of Ag^+ to Ag onto gold disk electrode from 50 mmol L^{-1} AgTfO in [EMIM]TfO or in $[HMIM^+][HSO_4^-]$. The reduction peak potential (E_p^{red}), the oxidation peak potential (E_p^{ox}), the midpoint potential (E_m), the peak to peak separations (ΔE_p^{ox-red}), the reduction charge (Q_{red}), the oxidation charge (Q_{ox}) and the charge efficiency (Q_{ox}/Q_{red}) are displayed for each scan rate. The values of E_p^{red} shifted to more negative potentials with the increase of scan rate for both ILs, suggesting a nucleation process[8,41]. The charge associated with the stripping process to the reduction process (Q_{ox}/Q_{red}) in $[HMIM^+][HSO_4^-]$ was always less than one, which suggests that the removal of silver from gold surface is not a fully electrochemically reversible process, whereas in

[EMIM]TfO the Q_{ox}/Q_{red} was around one, indicating that the removal of silver from gold surface is a fully chemically reversible process[8,21].

All the electrochemical measurements were carried out *versus* Ag reference electrode, which is a quasi-reference electrode (QRE)[42]. Thus, the potential of the QRE can suffer dynamic changes during the time period when the Ag wire is immersed in the IL system during, or even as a consequence of, the electrochemical measurement[42]. Therefore, the QRE needs to be calibrated against a suitable reference electrode or a standard redox compound to give a known reference electrode potential. In this study, the potential of the redox couple ferrocene/ferrocenium (Fc/Fc^+) was measured in the employed ILs. Since electrodepositions of silver were made in different temperatures, it was necessary to verify if the increase of temperature would induce a change in the potential of Ag wire, which would become the potential of the electrochemical measurement unreliable. Thus, the potential of the redox couple Fc/Fc^+ was measured at different temperatures, varying from 25 °C to 45 °C, in the employed ILs. Table 2 shows the formal reference potentials (E') for ferrocene cyclic voltammograms at different temperatures.

Table 2

The formal reference potentials (E') were calculated based on Saheb *et al.* report[27]. The value of E' for ferrocene is almost independent of the temperature, pointed out that the potentials of the electrochemical measurements in this temperature range are reliable.

Cyclic voltammograms were recorded in several temperatures (from 25 °C to 45 °C), to verify the electrochemical behaviour of AgTfO in [EMIM]TfO (Fig. 3a) or in $[HMIM^+][HSO_4^-]$ (Fig. 3b) as a function of the temperature, over a scan rate of 50 mV s^{-1}. The temperature increase does not affect the reduction potential for both ILs. The reduction peaks appear in the same potentials (E_p^{red}), whereas the oxidation peak potentials (E_p^{ox}) shifted to less positive potentials. Nevertheless, the reduction and the oxidation current peaks increased for both ILs

(insets in Figs. 3a and 3b). The increase in the temperature causes a decrease in viscosity of ILs, which affect the values of D, but apparently, does not affect the redox potential[42,43].

Figure 3

3.2. Physical characterisation

Figs. 4a and 4b shown the SEM micrographs of Ag electrodeposited coatings obtained applying 30 mA cm^{-2} from the [EMIM]TfO IL on gold substrate at 45 °C. The Ag deposited exhibits a uniform distribution of spherical-like particulates containing large agglomerated crystallite clusters (Fig. 4a). Furthermore, a high magnification SEM micrograph, in Fig. 4b, revealed that the clusters are composed of nanometre Ag nuclei crystals with size in order of 50-200 nm in diameter.

Therefore, the Ag electrodeposition in [EMIM]TfO can be describe by two stages, in the first one, nanometre Ag crystal grains are formed, afterwards, these grains growing to form the agglomerated crystallites clusters, as already suggested by Abedin *et al.*[8] to the electrodeposition of Ag films using a [EMIM]TfO IL. The regular size distribution of Ag clusters (SEM images in Fig. 4) strongly evidence a nucleation-growth mechanism, which is in agreement with cyclic voltammetry data previously discussed in Table 1.

The granular morphology and the increase of the clusters sizes with temperature increase of the Ag deposits from [EMIM]TfO, observed in both Fig. 4a-b and Fig. S2a-c (ESI†), are similar to the data reported by Ispas *et al.*[19] that studied the Ag electrodeposition from [EMIM]TfO containing several concentration of Ag and at different temperatures. These researchers concluded that the Ag grains size increased mainly with the temperature increase, probably due to improved mass transport towards the electrode[19]. Basile *et al.*[21] also found that the Ag electrodeposition mechanism proceeded through by instantaneous nucleation-

growth mechanism in ILs medium onto GC substrate electrode. In addition, no expressive influence of current density and the temperature in morphology of Ag coatings obtained from [EMIM]TfO containing AgTfO on gold substrate were observed, see Fig. S2a-c (ESI†).

Figure 4

On the other hand, significant effects of both the current density and temperature on morphology of Ag deposits were observed when used the $[HMIM^+][HSO_4^-]$ IL. Fig. 5 shows a SEM micrograph of the Ag deposits with a dendrite morphology and fractal-like grown obtained by galvanostatic deposition at 15 mA cm^{-2} from $[HMIM^+][HSO_4^-]$ at 30 °C. In contrast, Ag deposits showing columnar bars morphology were observed at 45 °C at the same current density (Fig. S3a in the ESI†).

Figure 5

Furthermore, Ag deposits exhibiting dendrite fractal-like and columnar bars morphologies coexisting onto Au electrode were obtained at 30 mA cm^{-2} and 30 °C (Fig. 6a). High magnification SEM images revealed that dendrite morphology consists of very fine and well-defined branches in nanometre size which carry on growing,[29] as displayed in Fig. 6b. Otherwise, high magnification revealed columnar bars with average size ~4 μm in length, in Fig. 6c. When the temperature was increased to 45 °C, similar dendrite fractal-like and columnar bars morphologies coexisting onto Au electrode were also observed, see Fig. S3b (ESI†).

The initial stages of formation of both dendrite and columnar morphologies were recorded by SEM micrographs in Figs. 6d and 6e. Both dendrite and columnar bar structures were grown in nuclei form of around 100 nm. Fig. 6d shows that some of these nuclei remain island formed. However, many of them elongated and evolve toward nanometre ramified branches to form the dendrite morphology like fractal structure (Fig. 6d). This Ag fractal structure formation is similar to the described by Drozdowicz-Tomsia *et al*.[44] to Ag dendrites

grow on silicon wafers. Otherwise, most of these nuclei do not evolve such braches, therefore, generating the columnar bar morphology (Fig. 6e).

EDS analysis revealed that the chemical composition of the deposited nanostructures obtained by galvanostatic method consists in only pure Ag, thus demonstrating the feasibility of the method to depositing pure Ag (Fig. S1a in the ESI†).

Figure 6

XRD experiments were carried out for the determination of crystallinity of Ag coatings as well as the probable formation of other phases different than pure Ag. Fig. 7(a-b) shows the XRD patterns of Ag deposits obtained at 30 mA cm^{-2} from $[HMIM^+][HSO_4^-]$ and from [EMIM]TfO on GC electrode at 30 and 45 °C, respectively. XRD pattern of GC substrate can be found in Fig. S4 in ESI†. The XRD pattern of as-deposited Ag coating from $[HMIM^+][HSO_4^-]$ showed characteristic diffraction peaks at 2θ = 37.8° and 64.3° which correspond to the diffraction of (111), and (220) crystal planes of face centred cubic (FCC–JCPDS # 64 706) polycrystalline Ag (Fig. 7a), which are in good agreement of previous studies[8,21]. Similar XRD pattern obtained for Ag deposits from [EMIM]TfO is show in Fig.7b.

The XRD pattern obtained by Ag electrodeposited from $[HMIM^+][HSO_4^-]$ revealed more intense (111) signal compared to the [EMIM]TfO. This suggests that the Ag layer electrodeposited from $[HMIM^+][HSO_4^-]$ is more oriented, as previously observed for the dendrite and columnar bar structures obtained by using this IL (Figs. 5 and 6). The intensity of the FCC Ag peaks was lower than to the GC substrate ones due to the very thin thickness of the coatings. The full width at half maximum (FWHM) of diffraction peak is related with crystallite size (d) by the Scherrer's equation[45]:

$$d = \frac{0.9\lambda}{\beta \cos\theta} \quad (1)$$

where λ is the wavelength of the incident radiation (1.5406 Å), β is the FWHM and θ is the Bragg angle[45]. Therefore, according to Scherrer's equation the average of crystallite size of

Ag was estimated to be ~42.6 and ~25.6 nm obtained from [$HMIM^+$][HSO_4^-] and [EMIM]TfO, respectively.

Figure 7

3.3. Molecular dynamics simulations

In order to get an atomistic picture of the differences between the ionic liquids with respect to their interactions with Ag^+ ions, molecular dynamics (MD) calculations in the NPT ensemble were performed.

Self-diffusion coefficient (D_{self}) of Ag^+ ions in both ILs were obtained from the mean square displacements (MSD) computed using MD by using Einstein relation:

$$D_{self} = \left[\frac{1}{6t} \left\langle \Delta^2 r(t) \right\rangle \right]_{t \to \infty} \quad (2)$$

where t is the simulation time and r(t) is the radius as a function of the simulation time.

Ag^+ ions reached their diffusive regime in both ILs after a few nanoseconds of simulation time. Ag^+ took longer to reach this regime due to its lower mobility in [$HMIM^+$][HSO_4^-]. D_{self} values were calculated through a linear fitting of the MSD curve in diffusive regime yielding $1.73\times10^{-9} \pm 0.24\times10^{-9}$ (fitting from 10 to 30 ns) and $2.62\times10^{-10} \pm 0.91\times10^{-10}$ cm^2 s^{-1} (fitted between 30 and 50 ns) for [EMIM]TfO and [$HMIM^+$][HSO_4^-], respectively. Our results are shown in Fig. 8. These findings are in good agreement with the experimental electrochemical observations presented previously in this work (Table 1). This agreement speaks in favour of the model used for describing ILs and their interaction with Ag^+.

Figure 8

As observed for fullerene in ILs[46], a wealth of information can be extracted from the energetic balance of interactions between the ionic liquids and their solute. The presence of AgTfO in both liquids causes a perturbation whose impact can be assessed through the

difference between the interactions in pure liquid and in solution. The energetic impact expressed as Coulomb and Lennard-Jones potential energy terms ($\Delta U_{Coul} + \Delta U_{LJ}$) for these interactions (Table S1) is positive (destabilizing), but larger by 92 kJ mol^{-1} for [EMIM]TfO. As expected, the Ag^+ ion has a strong interaction in both liquids being –374.5 $kJ.mol^{-1}$ for [$HMIM^+$][HSO_4^-] and –384.3 for [EMIM]TfO. Therefore MD results suggests that dissolving AgTfO is energetically more favourable in [$HMIM^+$][HSO_4^-]. These strong interactions are consistent with the lower mobility of Ag in [$HMIM^+$][HSO_4^-].

Comparing the Ag-Ag radial distribution function (G(r)) computed over 100 ns molecular dynamics calculations revealed some interesting features (Fig. S5). The Ag^+ distribution in [$HMIM^+$][HSO_4^-] is more structured than in [EMIM]TfO as can be seen from the highs of the first and second G(r) peaks. This enhanced structure in [$HMIM^+$][HSO_4^-] is probably related to the better Ag deposition properties of [$HMIM^+$][HSO_4^-] over [EMIM]TfO.

With the aid of the computational simulations, it was possible to corroborate the experimental results for D_{self}, and to link this difference to fundamental properties of both LIs AgTfO solutions. Results indicate that, despite their structural similarities, these two liquids behave in very distinct ways with respect to their interaction with a silver salt, with [$HMIM^+$][HSO_4^-] producing a more structured Ag distribution that is energetically very stable.

Figure 9

4. Conclusions

This paper shows that air and water stable ILs can be used as promising baths to replace toxic electroplating baths for silver electrodeposition. The electrodeposition of silver onto gold electrodes was investigated in two different ILs, [EMIM]TfO and [$HMIM^+$][HSO_4^-]. The voltammetric data obtained for both systems show that silver electrodeposition is a

diffusion-controlled process. These data also shows that Ag^+ ion has higher mobility in [EMIM]TfO than in [$HMIM^+$][HSO_4^-], which can be related to its viscosity and/or to the stronger interaction of Ag^+ with HSO_4^- than with TfO, as shown by MD simulations. The determination of the diffusion coefficient values for complex systems are indispensable to chemical research and by the methodology presented here it was possible to observe that the simulations results are in good agreement with experimental results. Moreover, the voltammetric data also shows evidence that the electrodeposition of Ag would proceed via a nucleation and growth mechanism. This mechanism was confirmed by SEM analysis. The deposited Ag exhibits a uniform distribution of spherical particulates containing large agglomerated crystallites clusters in [EMIM]TfO for all investigated conditions. On the other hand, Ag coatings morphologies in [$HMIM^+$][HSO_4^-] evolving from dendrites at 15 mA cm^{-2} to the coexistence of dendrites and columnar shapes at 30 mA cm^{-2}. The Ag coatings were deposited as FCC polycrystalline Ag with crystallite size in nanometre scale.

References

1 B. H. R. Suryanto, C. a. Gunawan, X. Lu and C. Zhao, *Electrochim. Acta*, 2012, **81**, 98–105.

2 M. Schlesinger and M. Paunovic, *Modern Electroplating*, Wiley, New York, NY, 4th edn., 2000.

3 W. Simka, D. Puszczyk and G. Nawrat, *Electrochim. Acta*, 2009, **54**, 5307–5319.

4 F. Endres, *ChemPhysChem*, 2002, **3**, 144–154.

5 F. Endres, D. R. MacFarlane and A. Abbott, *Electrodeposition from Ionic Liquids*, Wiley-VCH, Weinheim, 2008.

6 R. Fukui, Y. Katayama and T. Miura, *J. Electrochem. Soc.*, 2011, **158**, D567.

7 J. M. Reyna-González, J. C. Reyes-López and M. Aguilar-Martínez, *Electrochim. Acta*, 2013, **94**, 344–352.

8 S. Zein El Abedin and F. Endres, *Electrochim. Acta*, 2009, **54**, 5673–5677.

9 J. S. Wilkes, 2004, **214**, 11–17.

10 Y. Li, Q. Qiang, X. Zheng and Z. Wang, *Electrochem. commun.*, 2015, **58**, 41–45.

11 S. Caporali, P. Marcantelli, C. Chiappe and C. S. Pomelli, *Surf. Coatings Technol.*, 2015, **264**, 23–31.

12 A. B. Patil and B. M. Bhanage, *Phys. Chem. Chem. Phys.*, 2014, **16**, 3027–35.

13 T. L. Greaves and C. J. Drummond, *Chem. Rev.*, 2008, **108**, 206–237.

14 H. Ohno, *Aspects of Ionic Liquids Aspects of Ionic*, Wiley, 2nd edn., 2011.

15 W. Xu and C. A. Angell, *Science*, 2003, **302**, 422–425.

16 M. Anouti, J. Jones, A. Boisset, J. Jacquemin, M. Caillon-caravanier and D. Lemordant, *J. Colloid Interface Sci.*, 2009, **340**, 104–111.

17 Y. Shen, D. F. Kennedy, T. L. Greaves, A. Weerawardena, R. J. Mulder, N. Kirby, G. Song and C. J. Drummond, *Phys. Chem. Chem. Phys.*, 2012, **14**, 7981.

18 J. M. Reyna-González, R. Galicia-Pérez, J. C. Reyes-López and M. Aguilar-Martínez, *Sep. Purif. Technol.*, 2012, **89**, 320–328.

19 A. Ispas, M. Pölleth, K. H. T. Ba, A. Bund and J. Janek, *Electrochim. Acta*, 2011, **56**, 10332–10339.

20 R. Bomparola, S. Caporali, A. Lavacchi and U. Bardi, *Surf. Coatings Technol.*, 2007, **201**, 9485–9490.

21 A. Basile, A. I. Bhatt, A. P. O'Mullane and S. K. Bhargava, *Electrochim. Acta*, 2011, **56**, 2895–2905.

22 P. He, H. Liu, Z. Li, Y. Liu, X. Xu and J. Li, 2004.

23 I. Kazeminezhad, a. C. Barnes, J. D. Holbrey, K. R. Seddon and W. Schwarzacher, *Appl. Phys. A Mater. Sci. Process.*, 2007, **86**, 373–375.

24 M. C. Tsai, D. X. Zhuang and P. Y. Chen, *Electrochim. Acta*, 2010, **55**, 1019–1027.

25 S. Schaltin, N. R. Brooks, L. Stappers, K. Van Hecke, L. Van Meervelt, K. Binnemans and J. Fransaer, *Phys. Chem. Chem. Phys.*, 2012, **14**, 1706.

26 C. Carlesi Jara, G. R. Salazar-Banda, R. S. Arratia, J. S. Campino and M. I. Aguilera, *Chem. Eng. J.*, 2011, **171**, 1253–1262.

27 A. Saheb, J. Janata and M. Josowicz, *Electroanalysis*, 2006, **18**, 405–409.

28 M. Parrinello and A. Rahman, *J. Appl. Phys.*, 1981, **52**, 7182–7190.

29 G. Bussi, D. Donadio and M. Parrinello, *J. Chem. Phys.*, 2007, **126**, 7182–7190.

30 N. C. Lopes and B. Pascal, *J. Phys. Chem. B*, 2004, **108**, 16893–16898.

31 J. N. Canongia Lopes, J. Deschamps and A. A. H. Pádua, *J. Phys. Chem. B*, 2004, **108**, 2038–2047.

32 K. Shimizu, *J. Phys. Chem. B*, 2008, **112**, 5039–5046.

33 W. L. Jorgensen, D. S. Maxwell and J. Tirado-rives, *J. Am. Chem. Soc.*, 1996, **118**, 11225–11236.

34 B. Schwenzer, S. N. Kerisit and M. Vijayakumar, *RSC Adv.*, 2014, **4**, 5457–5464.

35 C. M. Breneman and K. B. Wiberg, *J. Comput. Chem.*, 1990, **11**, 361–373.

36 R. Spezia, C. Nicolas, A. Boutin and R. Vuilleumier, *Phys. Rev. Lett.*, 2003, **91**, 208304.

37 A. R. Leach, *Molecular Modelling: Principles and Applications*, Prentice Hall, 2001.

38 B. Hess, H. Bekker, H. J. C. Berendsen and J. G. E. M. Fraaije, *J. Comput. Chem.*, 1997, **18**, 1463–1472.

39 T. Darden, D. York and L. Pedersen, *J. Chem. Phys.*, 1993, **98**, 10089–10092.

40 H. J. C. Berendsen, D. van der Spoel and R. van Drunen, *Comput. Phys. Commun.*, 1995, **91**, 43–56.

41 A. I. Bhatt and A. M. Bond, *J. Electroanal. Chem.*, 2008, **619-620**, 1–10.

42 A. A. J. Torriero, J. Sunarso and P. C. Howlett, *Electrochim. Acta*, 2012, **82**, 60–68.

43 M. Matsumiya, M. Terazono and K. Tokuraku, *Electrochim. Acta*, 2006, **51**, 1178–1183.

44 K. Drozdowicz-Tomsia, F. Xie and E. M. Goldys, *J. Phys. Chem. C*, 2010, **114**, 1562–1569.

45 B. Cullity and S. Stock, *Elements of X-ray Diffraction*, 2001.

46 C. Maciel and E. Eterno, *Chem. Phys. Lett.*, 2013, **568-569**, 75–79.

Figure captions

Fig. 1. Cyclic voltammograms taken on gold disk electrode for: (a) pure [EMIM]TfO (dash line,peaks a and b are the redox processes related to the substrate) and containing 50 mmol L^{-1} of AgTfO (solid line, peaks c and d are the Ag redox processes) and (b) pure [$HMIM^+$][HSO_4^-] (dash line) and containing 50 mmol L^{-1} of AgTfO (solid line). The experiments were conducted at room temperature using an Ag wire as the pseudoreference electrode. Scan rate 50 mV s^{-1}.

Fig. 2. Cyclic voltammograms taken on gold disk electrode for: (a) [EMIM]TfO containing 50 mmol L^{-1} AgTfO and (b) [$HMIM^+$][HSO_4^-] containing 50 mmol L^{-1} AgTfO, all recorded from 10 to 100 mV s^{-1} at room temperature. The insets show the linear dependence between the reduction peak current and the square root of the scan rate: $I_{rp} = -6.33\times10^{-6}\ \upsilon^{1/2} + 1.01\times10^{-7}$ with $R^2 = 0.9986$ and $I_{rp} = -1.84\times10^{-6}\ \upsilon^{1/2} + 4.93\times10^{-8}$ with $R^2 = 0.9999$.

Fig. 3. Cyclic voltammograms taken on gold disk electrode for: (a) [EMIM]TfO containing 50 mmol L^{-1} AgTfO and (b) [$HMIM^+$][HSO_4^-] containing 50 mmol L^{-1} AgTfO, all recorded in the temperature range from 25 to 45 °C. Scan rate 50 mV s^{-1}. The insets show the effect of the temperature on the values of the reduction and oxidation peak currents.

Fig. 4. FEG-SEM micrographs of Ag deposits obtained by galvanostatic deposition (30 mA cm^{-2}) from the IL [EMIM]TfO containing 50 mmol L^{-1} AgTfO on gold substrate at 45 °C. (a) low and (b) high magnification.

Fig. 5. SEM micrograph of Ag deposit obtained by galvanostatic deposition (15 mA cm^{-2}) from the IL $[HMIM^+][HSO_4^-]$ containing 50 mmol L^{-1} AgTfO on gold substrate at 30 °C.

Fig. 6. FEG-SEM micrographs of Ag deposits obtained by galvanostatic deposition (30 mA cm^{-2}) from the IL $[HMIM^+][HSO_4^-]$ containing 50 mmol L^{-1} AgTfO on gold substrate at 30 °C. (a) low magnification shows coexistence between columnar and dendrite morphologies, and high magnification show in details: (b) dendrite morphology, (c) columnar morphology, (d) initial stages of formation of dendrite and (e) columnar morphologies.

Fig. 7. XRD patterns of Ag deposits obtained on GC substrate by galvanostatic deposition at 30 mA cm^{-2} from the ILs: (a) $[HMIM^+][HSO_4^-]$ containing 50 mmol L^{-1} AgTfO at 30 °C and (b) [EMIM]TfO containing 50 mmol L^{-1} AgTfO at 45 °C.

Fig. 8. Mean square displacements (MSD) of Ag^+ ions in [EMIM]TfO (red) and $[HMIM^+][HSO_4^-]$ (blue) ILs.

Fig. 9. Spatial distribution functions of ions around Ag^+ (green): [EMIM] or $[HMIM^+]$ in blue, TfO in red, and HSO_4^- in grey. ILs indicated in the figure.

Tables

Table 1: Experimental voltammetric data for 50 mmol L^{-1} AgTfO in [EMIM]TfO or [$HMIM^+$][HSO_4^-] recorded on gold disk electrode using the same set-up as in Figs. 2a and 2b using a Ag wire as pseudoreference electrode

Scan rate ($mV\ s^{-1}$)	E_p^{red} (V)	E_p^{ox} (V)	E_m (V)	ΔE_p^{ox-red} (V)	Q_{red} (μC)	Q_{ox} (μC)	Q_{ox}/Q_{red}	D ($cm^2\ s^{-1}$)
Silver electrodeposition using the [$HMIM^+$][HSO_4^-] IL								
10	–0.054	0.060	0.003	0.114	38	35	0.92	
25	–0.060	0.065	0.003	0.125	25	23	0.92	3.1×10^{-10}
50	–0.062	0.079	0.009	0.141	20	19	0.95	
100	–0.071	0.085	0.007	0.156	14	13	0.93	
Silver electrodeposition using the [EMIM]TfO IL								
10	–0.118	0.206	0.044	0.324	242	242	1.00	
25	–0.131	0.214	0.041	0.345	154	154	1.00	3.6×10^{-9}
50	–0.152	0.221	0.035	0.373	108	108	1.00	
100	–0.162	0.235	0.037	0.397	778	772	0.99	

Table 2: Formal reference potentials for 2.5 mmol L^{-1} ferrocene obtained from voltammetric experiments at different temperatures using Ag wire as a pseudoreference electrode.

Temperature	[EMIM]TfO plus Fc	$[HMIM^+][HSO_4^-]$ plus Fc
(°C)	E' (V)	E' (V)
25	0.600	0.047
30	0.598	0.047
35	0.601	0.045
45	0.602	0.045

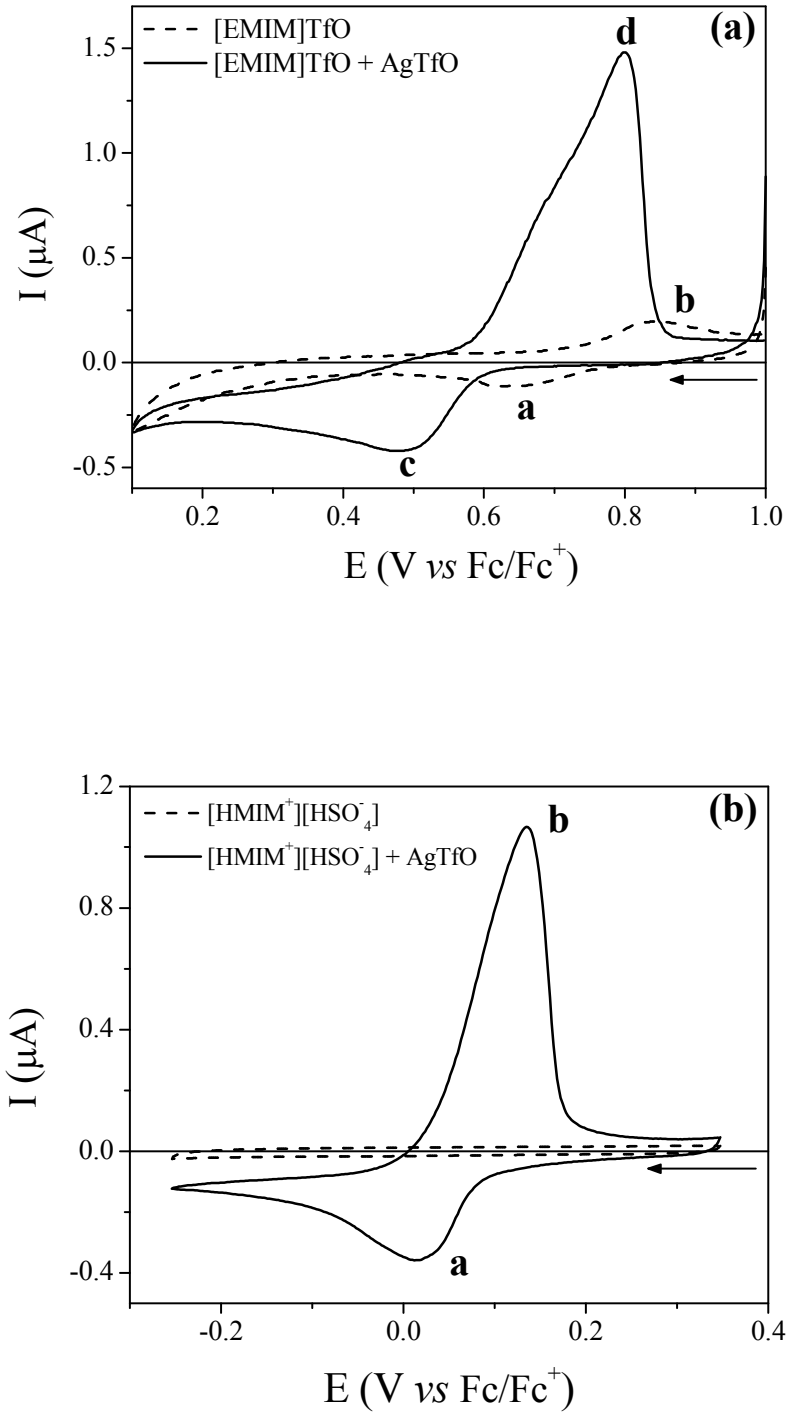

Fig. 1. *Figueredo-Sobrinho et al.*

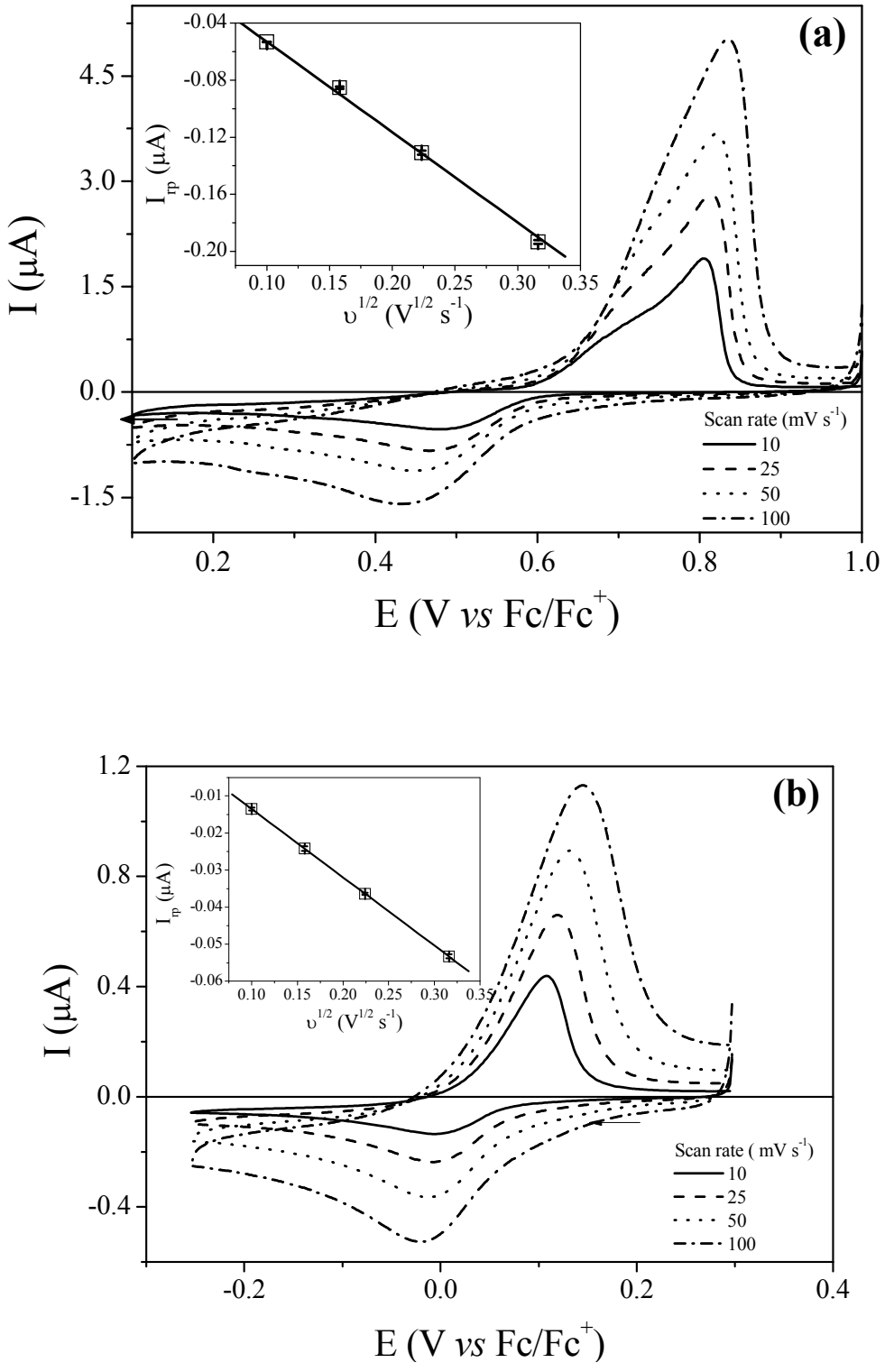

Fig. 2. *Figueredo-Sobrinho et al.*

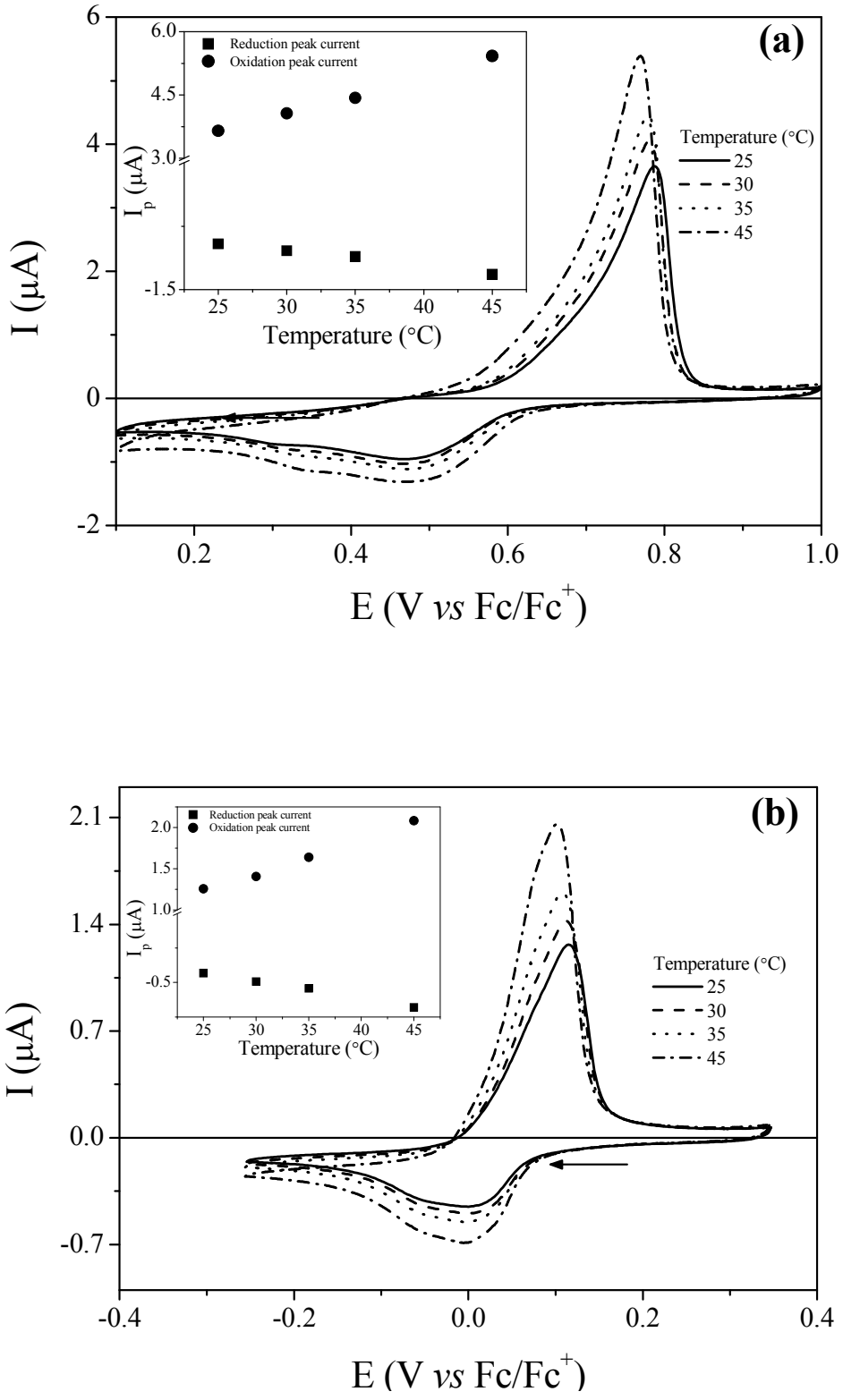

Fig. 3. *Figueredo-Sobrinho et al.*

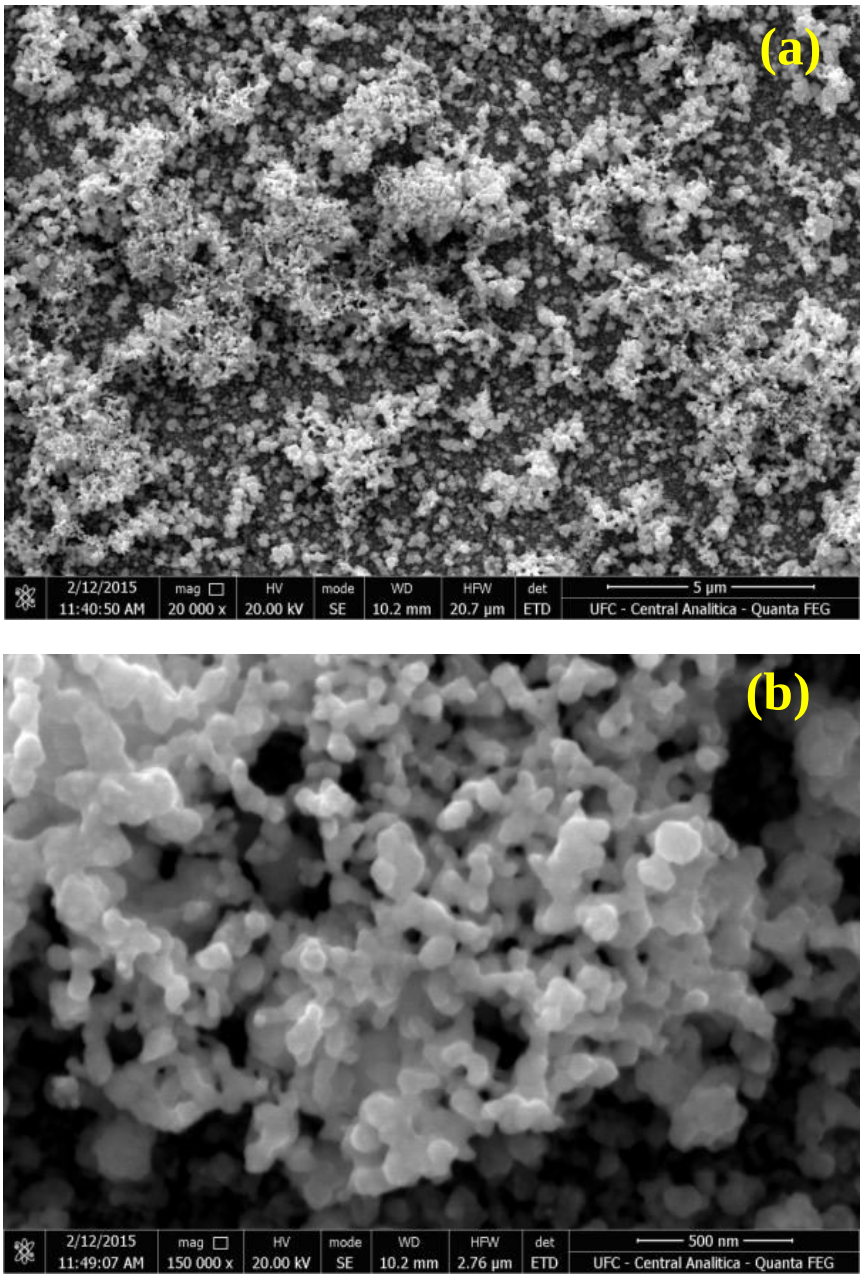

Fig. 4. *Figueredo-Sobrinho et al.*

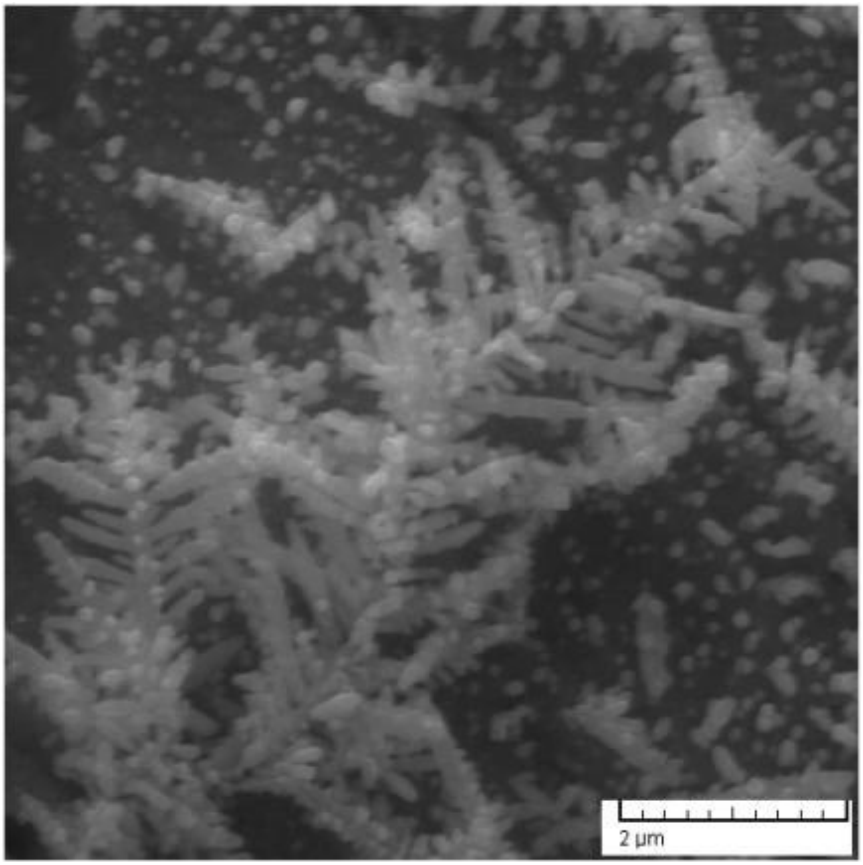

Fig. 5. *Figueredo-Sobrinho et al.*

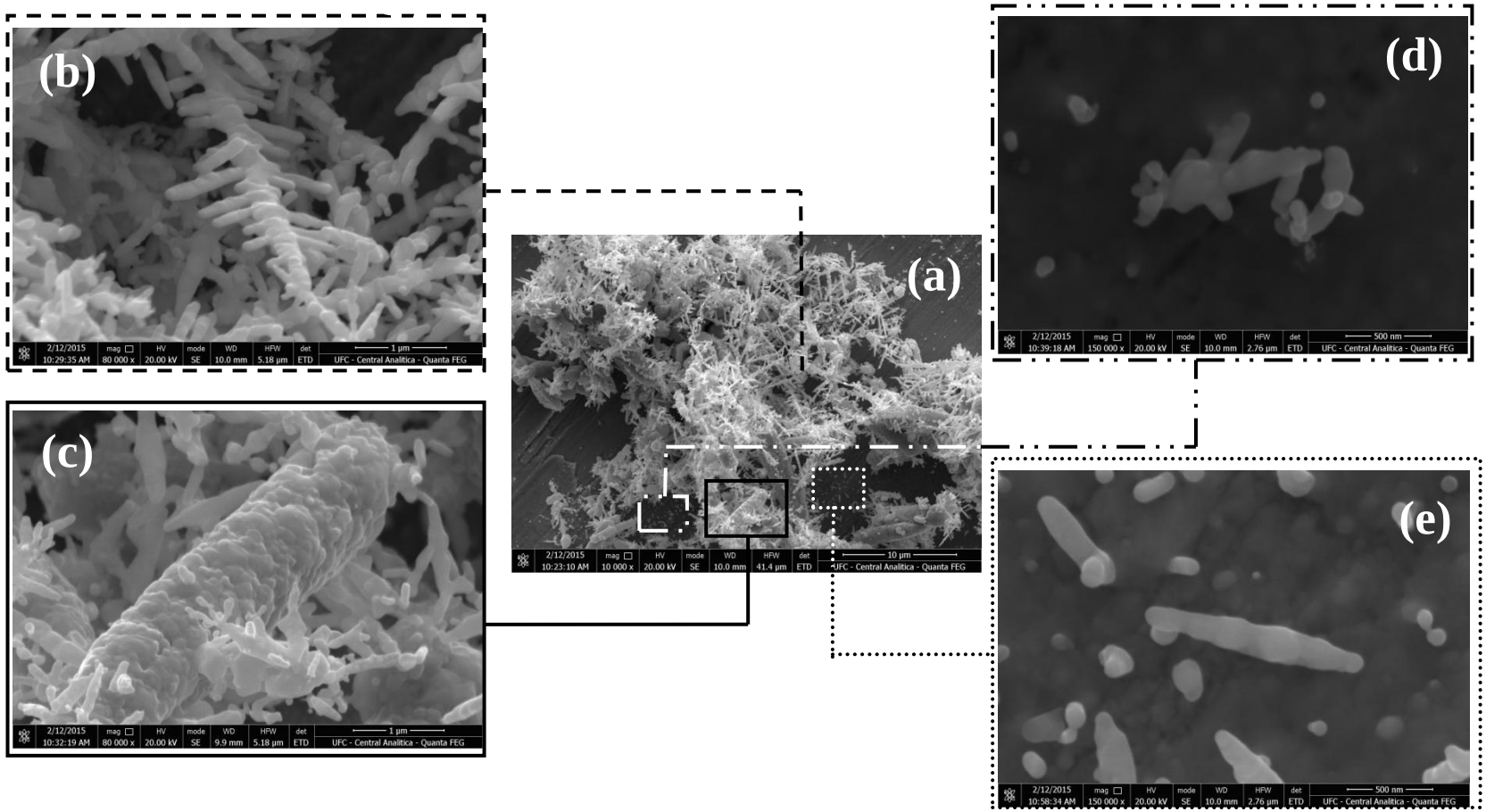

Fig. 6. *Figueredo-Sobrinho et al.*

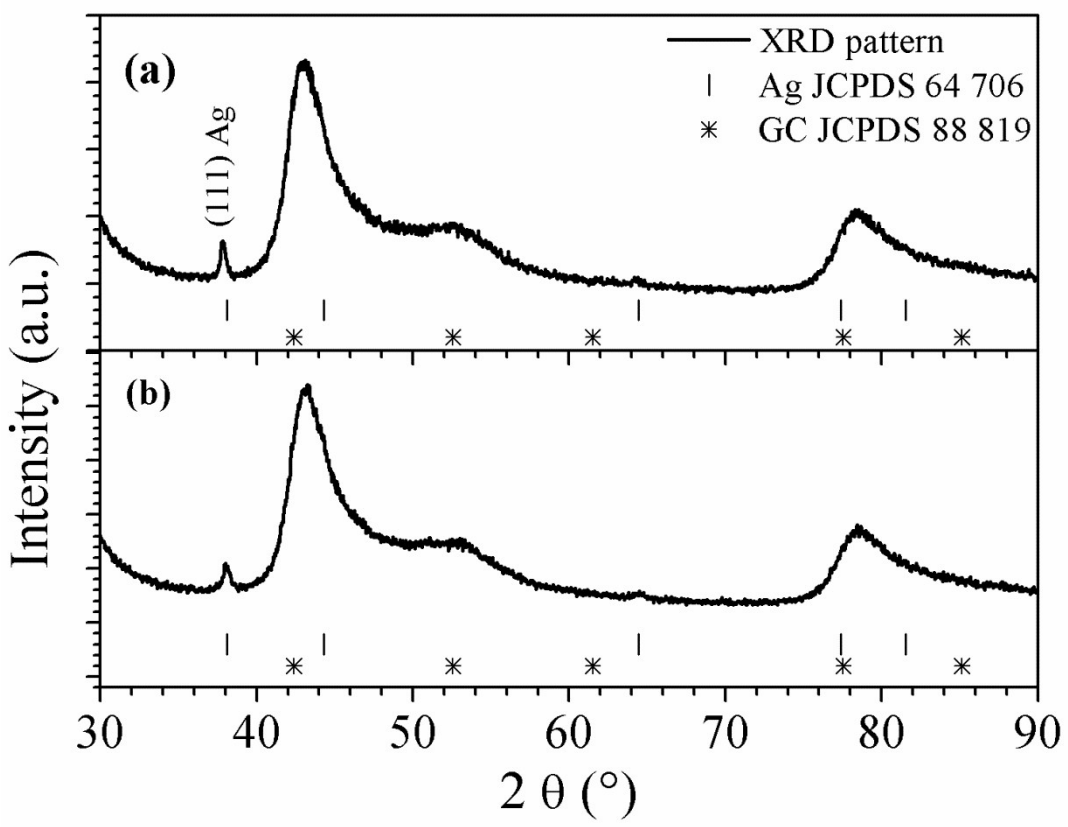

Fig. 7. *Figueredo-Sobrinho et al.*

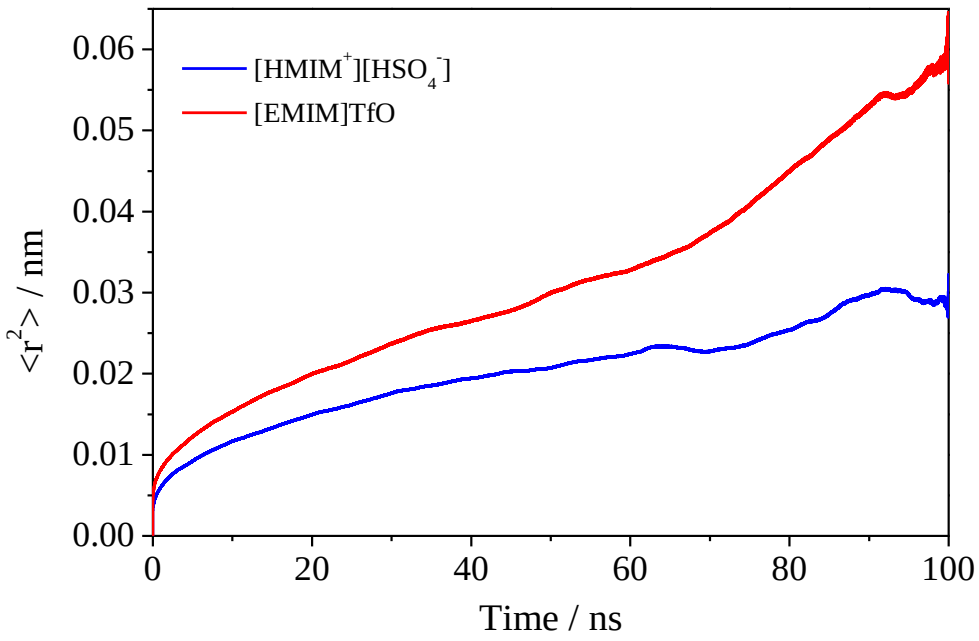

Fig. 8. *Figueredo-Sobrinho et al.*

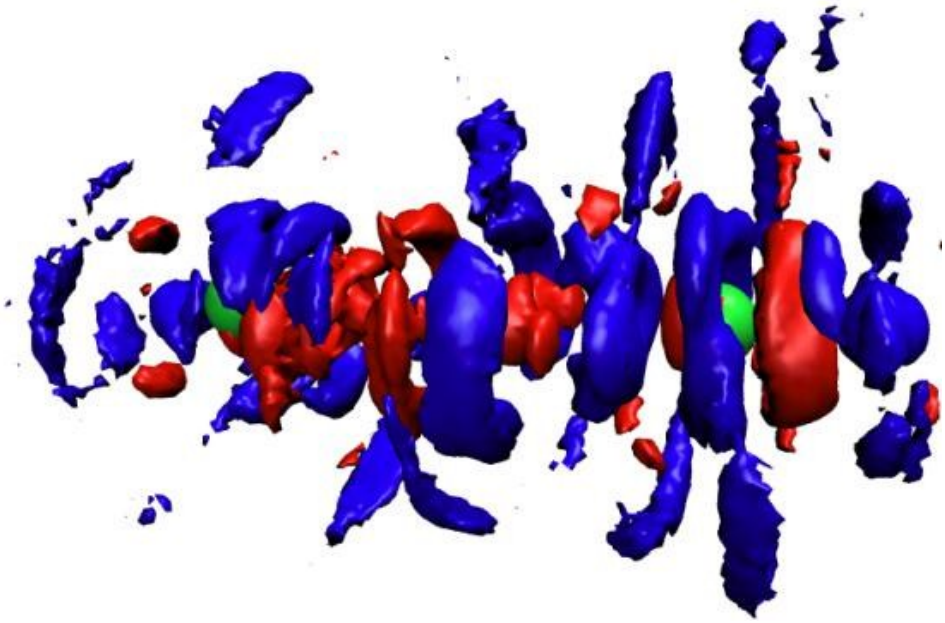

[EMIM]TfO

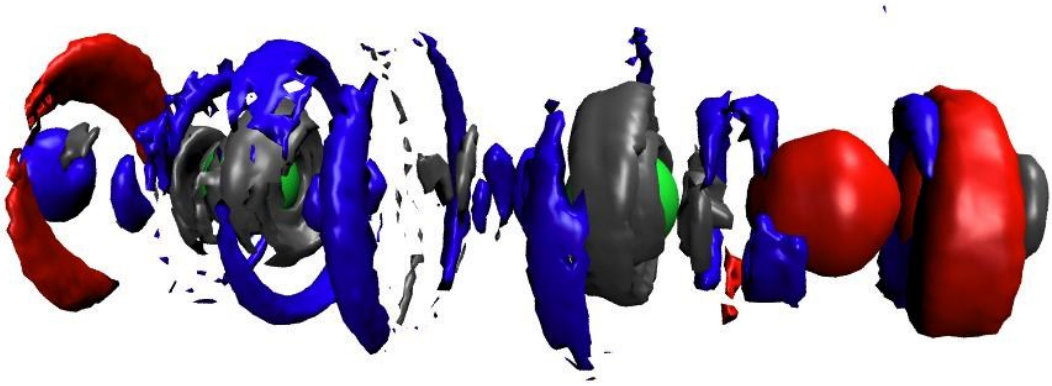

[HMIM^{+}][HSO$_4^{-}$]

Fig. 9. *Figueredo-Sobrinho et al.*